CHAPTER V

VISIBLE LIGHT SCATTERING PROPERTIES OF SILICA MICROPARTICLES

5.1 Introduction

Most non-contact characterization techniques of nonspherical particles basically use laser probes and high resolution visual imaging at different wavelengths [1-3]. Laser based probes are preferred due to the advantages of real time monitoring and particle sizing [2, 4, 5]. Spheroidal models are applied to study nonpherical aerosol properties mainly for small and moderate size parameters although it is difficult to achieve accuracy [6]. It is evident that well accepted numerical techniques and experimental results are not extensively available for higher size parameters [7]. For such particles volume integral techniques like DDA are the preferred numerical tool [8].

It is of utmost importance to study samples as analogues in situations where the real particles are inaccessible. Mainly the shape and size distribution of particles influence their physical properties and determine the utilities in medical and industrial applications [9-12].

Silica is one of the most abundant element in nature and earth's crust. Its presence has been also detected in extraterrestrial dust. It found a wide applicability ranging from industrial generation to drug delivery systems. Another important use of silica nanoparticle is the preparation of enhanced quality polymer nanocomposites [13-22]. PSD measurement of silica is also required in medical applications as it effects cell uptake process [23-26]. In indirect but significant applications, silica nanopowders are used in adsorbents, photonic devices (LEDs), optical fibers and waveguides [28-32] and thermal insulation [33].

Silica is extensively used in manufacturing industries like glass and pottery releasing a harmful level of particulate matter into the air. Such silica particles are a major threat to human health including high probability of silicosis [34]. Detection and monitoring of silica levels are important in such environments due to its direct health impact.

This chapter provides a detailed description of the theoretical and experimental light scattering studies of irregularly shaped silica microparticles.

5.2 Computational technique for particle sizing of silica microparticles

Light scattering experiments for particle sizing of irregular particles require rigorous numerical calculations considering the complex and combined effects of shape, surface roughness, fluffiness, porosity and aggregation states on measured quantities. Design of such a particle sizing technique is based on an efficient computational model followed by laboratory simulations and finally a comparative analyses with the experimentally acquired or observational results. The curve fitting of theoretical data with experimental ones provides conclusive evidence about unknown and unpredictable particles otherwise difficult to investigate at different wavelengths. The computational modeling of scattering events involves approximation of the scattering particle as a combination of various possible regular or irregular geometries and then fitting with particle size distribution functions (normal, lognormal, power law etc.). In the laboratory simulation at a particular wavelength the particle sizes and refractive index values are run as variables (within a particular range) using all possible values and combinations. The final result of this technique gives the most probable combinations of refractive index and particle size distributions that could produce the scattering patterns under investigation, from an unknown scattering particle in the experimental or observational process. Computational fits for the most probable values are chosen for further analyses during the material identification process and also to precisely determine the physical properties namely refractive index, shape, size, surface morphology of the material.

This work is used preferably to simulate Silica (SiO_2) samples considering it to be unknown and inaccessible. It's near impossible to determine the particle shape irregularities in a particle determination process for unknown scatterers when the particles are also distributed in sizes. So in order to make possible the particle detection and sizing, regular geometries are considered to deconvolute the experimental results and separate out the effects of shape, porosity and surface roughness from the principal variables refractive indices and particle sizes. But in case the particle is accessible with known shapes and morphological evidences, this technique developed on computational abilities of DDA provides a very strong complementary computational tool for fitting remote sensing data and

astrophysical observations. To achieve a good approximation of the particles shapes a mixture of spherical and nonspherical regular geometries are incorporated in order to account for influence of nonsphericity on measured scattering parameters and accuracy of the technique. The curve fitting technique is as follows,

$$Computational\ results \xrightarrow{\textbf{best fits including effects of physcial parameters}} Experimental\ data$$

The flowchart for the particle size and refractive index determination technique is provided in Figure 5.1. As the variables produce a computational scattering pattern it is matched with the experimental data for a best fit. Once achieved the best combinations of refractive index and particle sizes are found out. If one of the parameters is known it is relatively easier to calculate the other one and vice versa from the fitted curves.

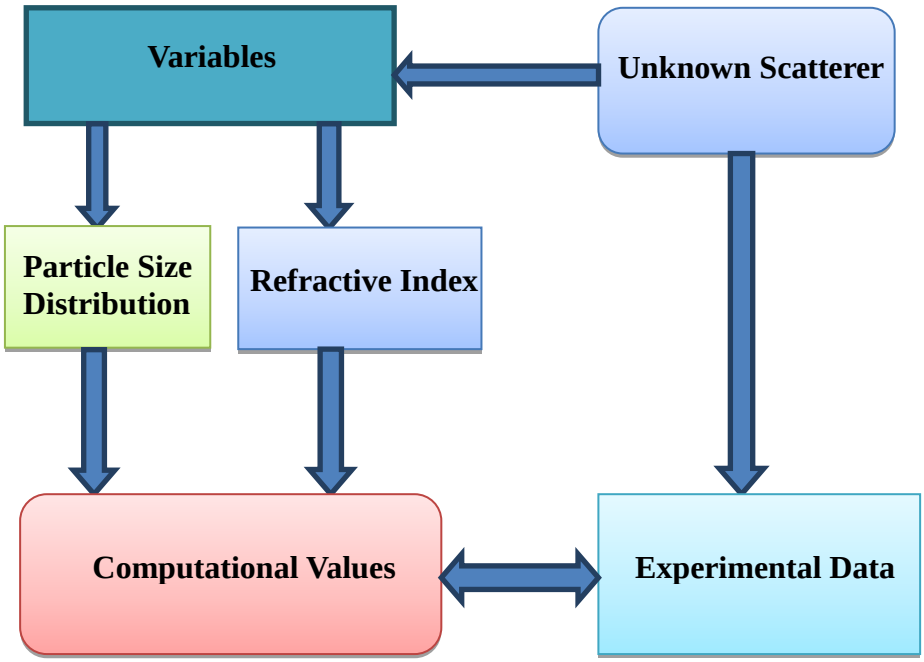

Figure 5.1 Flowchart of the particle sizing technique.

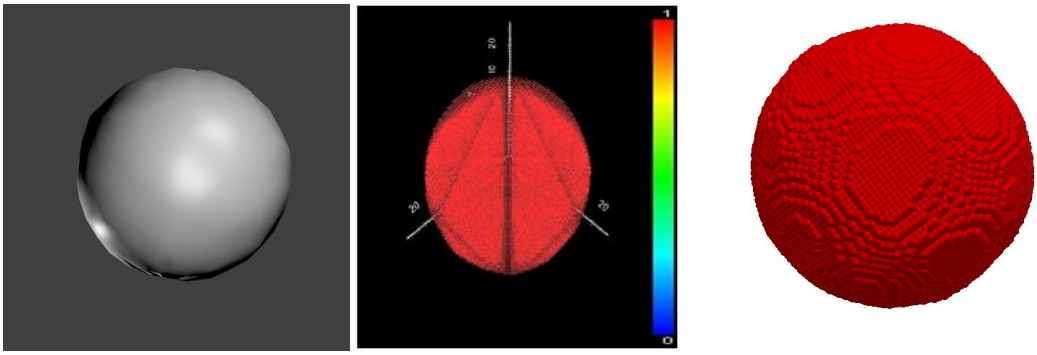

a **b** **c**

Figure 5.2 (a) Target model as a sphere (Shape1) in BLENDER3D, (b) Representation of target geometry as dipole arrays, (c) 3-D rendered dipole representation of the target.

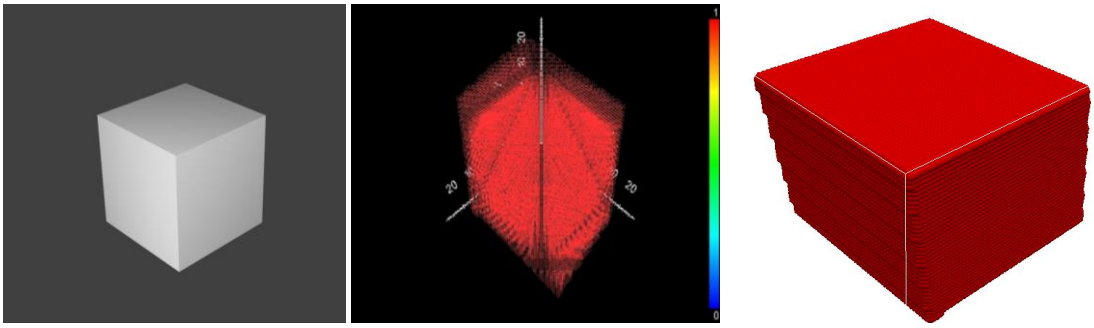

a **b** **c**

Figure 5.3 (a) Target model as a cube (Shape2) in BLENDER3D, (b) Representation of target geometry as dipole arrays, (c) 3-D rendered dipole representation of the target.

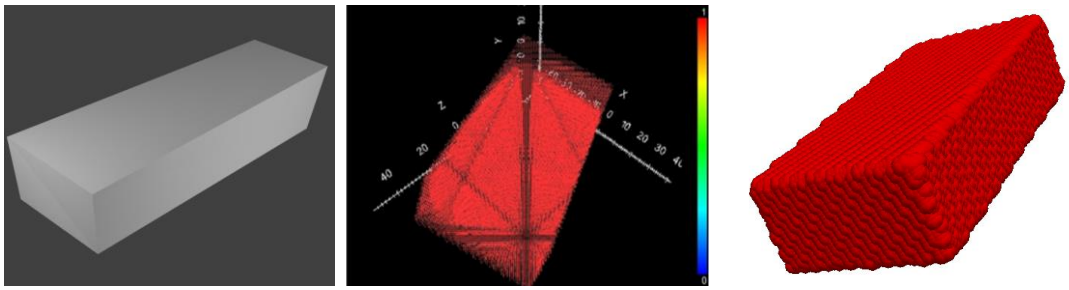

a **b** **c**

Figure 5.4 (a) Target model as a cuboid (Shape3) in BLENDER3D, (b) Representation of target geometry as dipole arrays, (c) 3-D rendered dipole representation of the target.

At first three particle shapes were generated [35, 36] in the computational model – spheres, cubes, and cuboids [with aspect ratios .33:1:2] referred as Shape1, Shape2 and Shape3 to account for all the dispersion and irregularities in particle shapes of the sample (Figure 5.2, 5.3 and 5.4). The target shapes are slightly deformed in steps by altering the positions of volumetric meshes to represent the surface roughness and small details. The representative targets are then converted into dipole arrays in DDSCAT Convert© by assigning 2×10^5 number of dipoles to each of the model volumes. The converted target geometries are used for calculation of scattering matrix elements and other parameters along with the normal variables refractive indices, wavelength, particle sizes, number of iterations and number of directions for carrying out averaging over orientations.

As the aim of this work is primarily particle sizing, the angular dependence in the forward scattering lobes of Mueller matrix elements is the most important factor that needs to be measured accurately [37]. In this case the angular dependence of size and shape averaged phase function ($F_{11}(\theta)$), and degree of linear polarization ($-F_{12}(\theta)/F_{11}(\theta)$) are measured both theoretically and experimentally. We tried to satisfy the condition upto a certain particle size at all the incident wavelengths after that it becomes difficult [38]. The values of maximum particle sizes are tabulated in Table 5.1.

Table 5.1 Maximum particle sizes and corresponding $|m|kd$ values for silica

Wavelength	Maximum particle size	Shape1	Shape2	Shape3
543.5 nm	2.00 µm	.9965	.9984	.9974
594.5 nm	2.15 µm	.9952	.9945	.9964
632.8 nm	2.30 µm	.9923	.9976	.9976

5.3 Physical properties of silica microparticles

The samples of silica microparticles used in the experimental characterization are acquired from sigma aldrich and then converted to a fine powder of a suitable range comparable to the incident laser wavelengths by grinding.

5.3.1 Particle size distribution

Based on the SEM micrographs and measurements, a Gamma size distribution function is employed to fit the particle size distribution of the sample. The size distribution and surface morphology of the samples are revealed by the high resolution images provided in Figure 5.5.

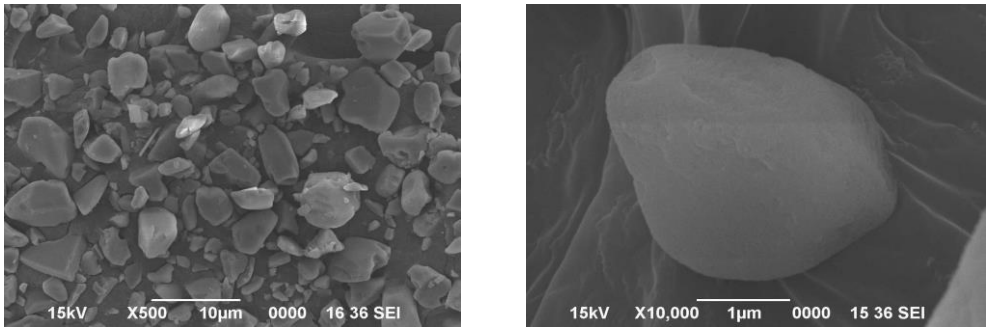

a **b**

Figure 5.5 Scanning Electron Micrography images of silica microparticles.

The gamma distribution function can be written as [39, 40],

$$n(x) = ax^{\alpha} \exp(-br) \qquad \textbf{5.1}$$

The values of normalization constants *a* and *b* are: $a = N\dfrac{b^{\alpha+1}}{\Gamma(\alpha+1)}$ and $b = \dfrac{\alpha}{x_m}$

In the above equation *x* is the particle radius, x_m is the modal radius of the distribution, Γ represents gamma function and α represents width of the size distribution.

The critical parameters of the size distribution function used to represent the sample is provided in Table 5.2 and shape of the function is shown in Figure 5.6.

Table 5.2 Critical parameters of Gamma size distribution function for silica

Size distribution parameters	Values used in computations.
Radius of particles (minimum)	0.35 μm
Radius of particles (maximum)	4.0 μm
Modal radius (x_m)	1.4 μm
Width of distribution (α)	0.3

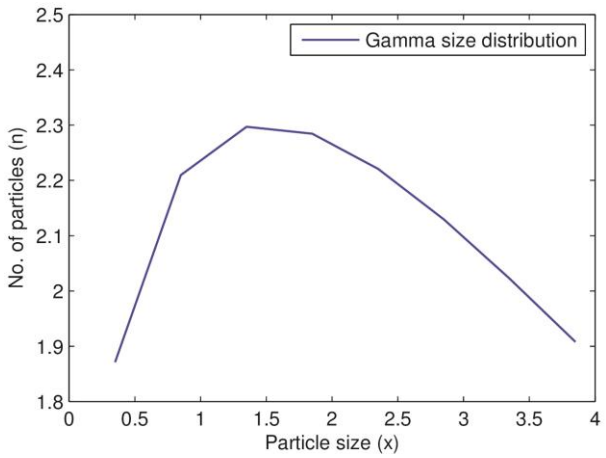

Figure 5.6 Particle size distribution function of silica microparticles.

5.3.2 Refractive index values of silica

The optical constants of silica (complex refractive index) used in the DDA computations are provided in Table 5.3 [41, 42].

Table 5.3 Refractive indices of silica at room temperature (25°C)

Wavelength	Refractive index (real) ***n***	Refractive index (imaginary) ***k***
543.5 nm	1.460078	0.00000010
594.5 nm	1.458404	0.00000010
632.8 nm	1.456704	0.00000010

5.4 Computed scattering parameters

The theoretical values of phase function $F_{11}(\theta)$ and degree of linear polarization $-F_{12}(\theta)/F_{11}(\theta)$ are computed along with the single scattering albedos (*a*) and asymmetry parameters (g).

5.4.1 Single scattering albedo (*a*) and Asymmetry parameter (g)

The single scattering albedo (*a*) can be calculated as $a = Q_{sca}/Q_{ext}$ **5.2**

where Q_{sca} is the scattering efficiency and Q_{ext} is the extinction efficiency.

And asymmetry parameter (g) is given by,

$g = \langle \cos\theta \rangle$ **5.3**

where θ is the scattering angle.

The calculated values at all three incident wavelengths and provided in Table 5.4.

Table 5.4 Single scattering albedo (a) and shape averaged asymmetry parameter (g) of silica

Wavelength	Single scattering albedo (***a***)	Asymmetry parameter (g)
543.5 nm	1	7.5938e-01
594.5 nm	1	7.9199e-01
632.8 nm	1	7.6823e-01

5.4.2 Comparative analyses of F_{11} and $-F_{12}/F_{11}$

The experimental values are measured using laboratory simulations in an experimental setup over the scattering angle range of 10^0 to 170^0 [43].

The accuracy of the measurements are ensured by repeating each set for a 100 times and subtracting out the background noise or the signal without scatterers. Also proper measures were taken to flush out any dust particles in the closed scattering chamber by using a suction pump which also ensures a steady sample flow into the scattering volume.

$$Signal_{(Corrected)} = Signal_{(Scatterer)} - Signal_{(Background)} \qquad \textbf{5.4}$$

A comparative study of the computational and experimental values shows good agreement in terms of general fitting of the scattering parameters. The Figure 5.7(a) and (b) shows the size averaged theoretical values of $F_{11}(\theta)$ and $-F_{12}(\theta)/F_{11}(\theta)$ for the three shape models along with the experimental results as reference for 543.5 nm wavelength, While the Figure 5.8(a) and (b) shows similar plots for 594.5 nm and Figure 5.9(a) and (b) for 632.5 nm wavelengths respectively. These analyses shows that the size averaged values of all the computational scattering parameters without averaging over shapes were unable to reproduce accurately the results obtained by experimental measurements. For instance the spherical shape shows close matches in a few cases at all the incident wavelengths while the other shapes cubes and cuboids deviates away significantly from the experimental curves, most obvious in case of $F_{11}(\theta)$, the cuboid shape deviating the maximum in each of the cases. Comparatively the theoretical results for $-F_{12}(\theta)/F_{11}(\theta)$ are relatively in a better agreement with those of the measured values, but with all the shapes deviating more or less from the reference experimental curve. This analyses basically reveals that that the phase function is a more sensitive function of shape irregularities and surface roughness while polarization is a dominant function of the particle size distribution and refractive index.

In DDA the target particle orientation is DDA is defined by using three angles in the target frame namely β, ϕ and θ. The orientational averaging may be achieved by running

the β and ϕ from 0^0 to 360^0 and θ from 0^0 to 180^0. In this computation the number of directions considered for averaging are 48 [7]. However this number of direction is not sufficient to achieve complete random orientation.

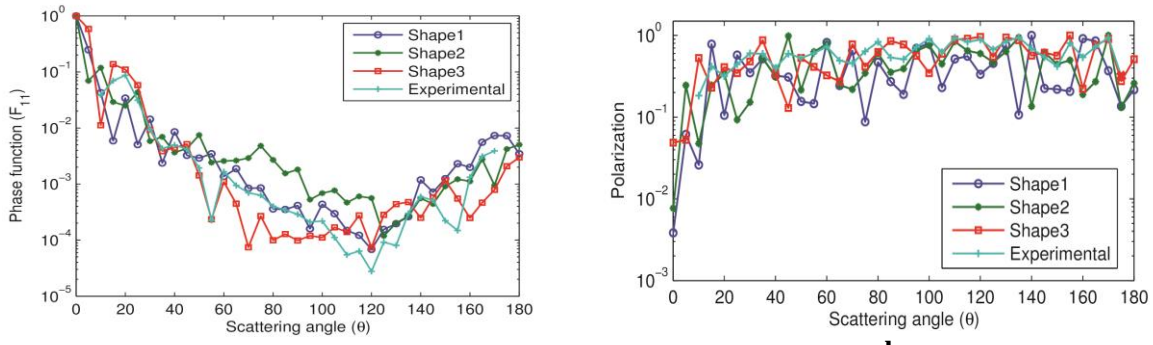

a **b**

Figure 5.7 (a) Size averaged computational values of phase function for the three model shapes and experimental values as reference, at 543.5 nm wavelength, (b) Plots for size averaged values of polarization and the experimental values at 543.5 nm wavelength.

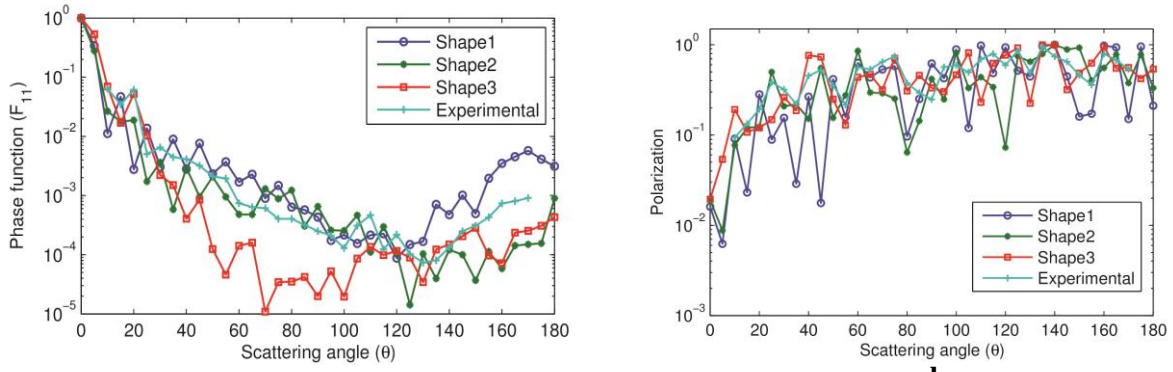

a **b**

Figure 5.8 (a) Size averaged computational values of phase function for the three model shapes and experimental values as reference, at 594.5 nm wavelength, (b) Plots for size averaged values of polarization and the experimental values at 594.5 nm wavelength.

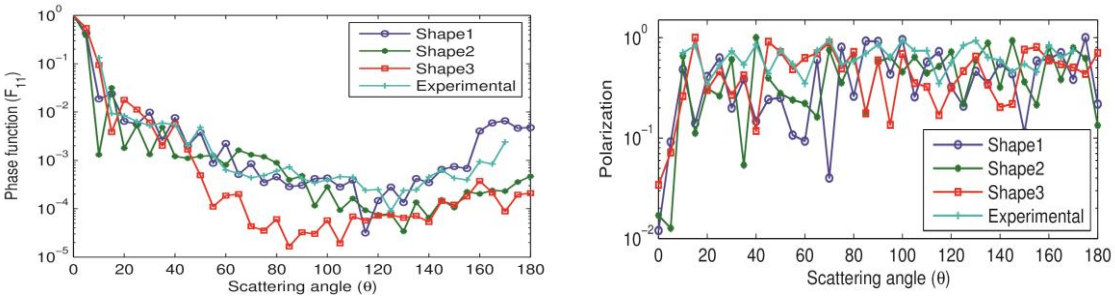

a **b**

Figure 5.9 (a) Size averaged computational values of phase function for the three model shapes and experimental values as reference, at 632.8 nm wavelength, (b) Plots for size averaged values of polarization and the experimental values at 632.8 nm wavelength.

5.5 Results and Discussions

As the size averaged values of the scattering parameters were not sufficient enough to reproduce the experimental results, shape averaging is required. In the final step, for conclusive evidences about accuracy and efficiency of the developed theoretical models shape averaging is performed over the already size averaged values of both the parameters. Figure 5.10(a) and (b) shows the comparative results of $F_{11}(\theta)$ and $-F_{12}(\theta)/F_{11}(\theta)$ for 543.5 nm, while Figure 5.11 (a) and (b) for 594.5 nm and similarly Figures 5.12 (a) and (b) for 632.8 nm respectively. After this addition to the modeling approach a reasonably better approximation to the experimental light scattering parameters of shape size distributed sample has been achieved. This provides an efficient way to measure the particle size distributions by separating out the effects of shape on the measured patterns. Among all the incident wavelengths, a near perfect match in case of phase function is achieved for 632.8 nm (which is relatively closer to the particle sizes as compared to the other wavelengths), most importantly a better fit in the forward scattering lobe upto a scattering angle of 45°. But it also deviates away from the experimental curve at mid and higher scattering angles upto 170°, the maximum measurement angle. This results shows that the phase function is more sensitive to the shape irregularities and surface roughness at wavelengths comparable to particle sizes. This can be bettered by considering majority of the irregular shapes present in

a laboratory sample. The polarization curves are near identical in all the cases throughout the whole scattering angle range. It can be concluded that also the shape averaging produces better results, but polarization is still a relatively less weak function of the particle shapes.

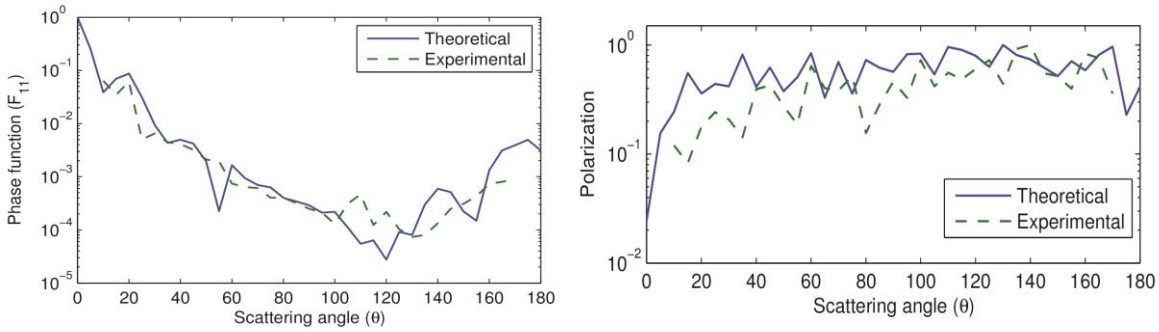

a **b**

Figure 5.10 (a) Shape and size averaged values of theoretical phase function and experimental values at 543.5 nm wavelength, (b) Shape and size averaged values of polarization and experimental values at 543.5 nm wavelength.

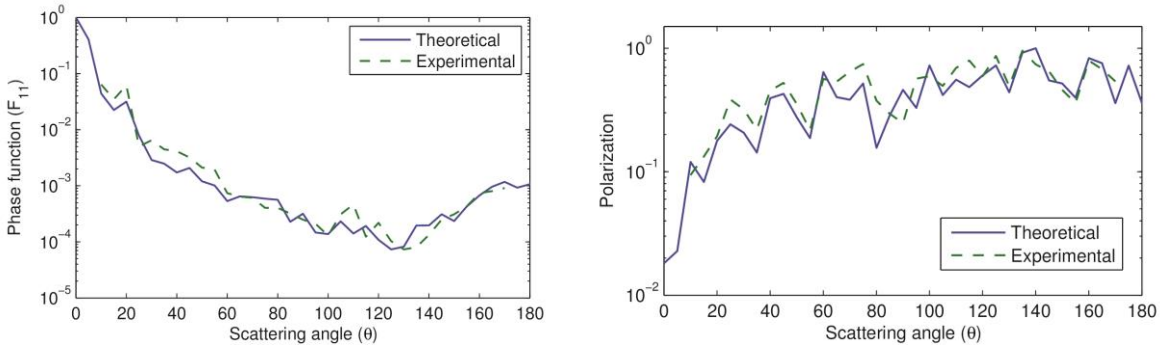

a **b**

Figure 5.11 (a) Shape and size averaged values of theoretical phase function and experimental values at 594.5 nm wavelength, (b) Shape and size averaged values of polarization and experimental values at 594.5 nm wavelength.

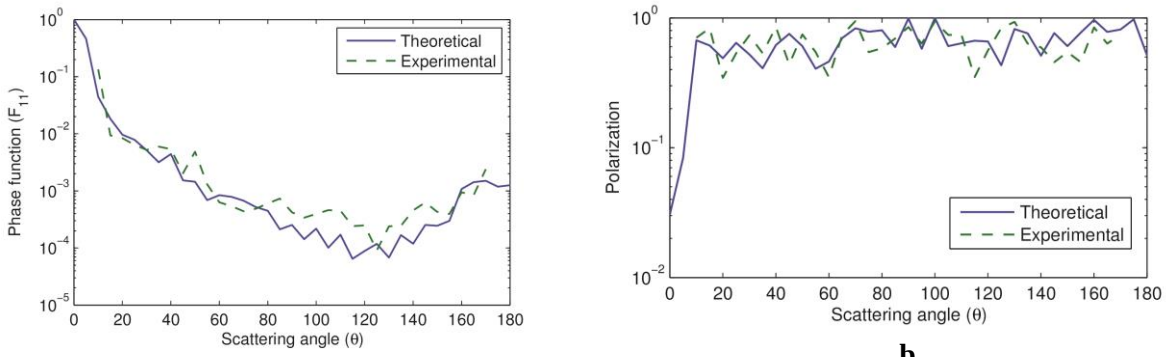

Figure 5.12 (a) Shape and size averaged values of theoretical phase function and experimental values at 632.8 nm wavelength, (b) Shape and size averaged values of polarization and experimental values at 632.8 nm wavelength.

Comparative studies are relatively easier for spherical and regularly shaped particles, where the shape effects are absent. But in this case the particles are highly irregular and lack any definite particle size distribution patterns. In our analyses the forward lobe of scattering matrix elements shows a typical characteristic shape, which is well reproduced in the computational model. But one thing must be pointed out that the curve fitting is average in the higher scattering angles or lower phase angles, i.e. extended to backward scattering directions. The overall match of the polarization values are quite reliable in describing the experimentally acquired data and are able to reveal the effects of nonspehricity and surface roughness in the observed scattering patterns. The discrepancies in modeling is due to the restrictions in using a large number of representative particle shapes. As evident from the visible evidences (SEM micrographs) this approach of considering regular nonspherical shape lacks the efficiency of realistic modeling. In some of our studies we have successfully reproduced the experimentally acquired light scattering patterns of highly irregular graphite and fayalite microparticles (dispersed in a wide size distribution range) [35, 36], with a higher degree of accuracy by realistically modeling the particle shapes based on the available visual evidences of the sample.

However this study is done with a different aim and approach more suitable to remote sensing studies involving unknown and unpredictable scatterers. In order to fulfil the purpose, a combination of regular shapes are used in the theoretical models. And the particle size distribution used in the computations provides a good approximation to the size

distribution of the laboratory sample although not accurate. To attain these conclusions the other variable parameters refractive index, surface roughness, number of dipoles, $|m|kd$ values etc. influencing the light scattering properties are very carefully chosen. It is known that terrestrial and cosmic dust particles and atmospheric aerosols produce observed spectra typical of highly irregular particles with porosity and fluffiness. A good model needs to account for most of the physical properties of scatterers. Our model is capable of producing the surface roughness effects by deforming the particle shape models (target geometries used in computations). The porosity and fluffiness of the samples are also accounted for by varying the number of dipoles from a range of 5×10^4 to 2×10^5 in steps of 5×10^4 dipoles and finally the most suitable value of 2×10^5 is selected which finally explains the experimental results with higher accuracies. This proves that higher the number of dipole better is the modeling approach to simulate the irregularities and roughness in the particulate samples. Similarly the density of the model geometries are also varied form a range of 1.0 to 2.0 in steps of 0.1 and a final value of 1.3 is selected. These final values of particle density, number of dipoles, particle size distribution used in combination with the regular shapes establishes the model. Most importantly the forwarding scattering lobe is enough in most cases to theoretically reproduce the experimental and observed results and also in predicting physical properties of unknown scatterers, provided we are unaware of the particle except any one of the physical parameters (mainly refractive index). Fixing the values of refractive index, a simulation is run for a range of particle size distribution and the closest match of the measured parameters are obtained for different combinations of size ranges. This gives a reliable approximation about the size distribution of samples dispersed in both shapes and sizes along with complex unpredictable physical properties.

5.6 Conclusions

1. This study provides an efficient way of detection and particle size distribution measurements for irregular micro and nanoparticles highly applicable in remote sensing, atmospheric, astrophysical, medical applications and also for finding

potential health hazards in the form of inhalable and respirable small particulate matter.

2. Better agreement is observed in the scattering parameters, provided the particle shapes fits the computational model.
3. This simulation is most effective for reproducing observational and experimentally measured optical light scattering properties of irregular particles with reasonably ordered structures similar to cuboids, cylinders and spheroids.
4. This work leads to the conclusion that the wavelengths closest to particle sizes provide the most appropriate approximation to irregular shapes.

References

1. Farmer, W.M., Measurement of particle size, number density, and velocity using a laser interferometer. *Applied Optics*, 11(11):2603-2612, 1972.
2. Black, D.L., McQuay, M.Q. and Bonin, M.P., Laser-based techniques for particle-size measurement: a review of sizing methods and their industrial applications. *Progress in energy and combustion science*, 22(3):267-306, 1996.
3. Zhong, W., Yu, A., Liu, X., Tong, Z. and Zhang, H., DEM/CFD-DEM modelling of non-spherical particulate systems: theoretical developments and applications. *Powder Technology*, 302:108-152, 2016.
4. Hnatovsky, C., Taylor, R.S., Simova, E., Bhardwaj, V.R., Rayner, D.M. and Corkum, P.B., High-resolution study of photoinduced modification in fused silica produced by a tightly focused femtosecond laser beam in the presence of aberrations. *Journal of applied physics*, 98(1):013517, 2005.
5. Wu, J., Chen, L., Yan, M., Wu, X., Gréhan, G. and Cen, K., Soot particle sizing based on analytical formula derived from laser-induced incandescence decay signals. *Applied Physics Letters*, 110(4):041903, 2017.
6. Dubovik, O., Holben, B.N., Lapyonok, T., Sinyuk, A., Mishchenko, M.I., Yang, P. and Slutsker, I., Non-spherical aerosol retrieval method employing light scattering by spheroids. *Geophysical Research Letters*, 29(10):54-1–54-4, 2002.
7. Nousiainen, T., Optical modeling of mineral dust particles: A review. *Journal of Quantitative Spectroscopy and Radiative Transfer*, 110(14-16):1261-1279, 2009.
8. Draine, B.T. and Flatau, P.J., Discrete-dipole approximation for scattering calculations. *JOSA A*, 11(4):1491-1499, 1994.
9. Ee, H.S., Kang, J.H., Brongersma, M.L. and Seo, M.K., Shape-dependent light scattering properties of subwavelength silicon nanoblocks. *Nano letters*, 15(3):1759-1765, 2015.
10. Champion, J.A., Katare, Y.K. and Mitragotri, S., Particle shape: a new design parameter for micro-and nanoscale drug delivery carriers. *Journal of Controlled Release*, 121(1-2):3-9, 2007.

11. Ma, Z., Merkus, H.G., de Smet, J.G., Heffels, C. and Scarlett, B., New developments in particle characterization by laser diffraction: size and shape. *Powder Technology*, 111(1-2):66-78, 2000.
12. Harvill, T.L. and Holve, D.J., In-Process Particle Size Distribution Measurements and Control. *Particle and particle systems characterization*, 10(5):262-265, 1993.
13. Rahman, I.A. and Padavettan, V., Synthesis of silica nanoparticles by sol-gel: size-dependent properties, surface modification, and applications in silica-polymer nanocomposites—a review. *Journal of Nanomaterials*, 2012:8, 2012.
14. Tielens, A.G. and Allamandola, L.J., Composition, Structure, and Chemistry of Interstellar Dust, *In Interstellar processes*, Springer Netherlands, pages 397-470, 1987.
15. Lisse, C.M., Chen, C.H., Wyatt, M.C., Morlok, A., Song, I., Bryden, G. and Sheehan, P., Abundant circumstellar silica dust and SiO gas created by a giant hypervelocity collision in the∼ 12 Myr HD172555 system. *The Astrophysical Journal*, 701(2):2019, 2009.
16. Rietmeijer, F.J., A cometary aggregate interplanetary dust particle as an analog for comet Wild 2 grain chemistry preserved in silica-rich Stardust glass. *Meteoritics and Planetary Science*, 44(10):1589-1609, 2009.
17. Ji, Y., Wang, H., Chen, J., Li, G., An, T. and Zhao, X., Can Silica Particles Reduce Air Pollution by Facilitating the Reactions of Aliphatic Aldehyde and NO2?. *The Journal of Physical Chemistry A*, 119(46):11376-11383, 2015.
18. Vallet-Regí, M. and Balas, F., Silica materials for medical applications. *The open biomedical engineering journal*, 2:1, 2008.
19. Barbe, C., Bartlett, J., Kong, L., Finnie, K., Lin, H.Q., Larkin, M., Calleja, S., Bush, A. and Calleja, G., Silica particles: a novel drug-delivery system. *Advanced materials*, 16(21):1959-1966, 2004.
20. Bariana, M., Aw, M.S. and Losic, D., Tailoring morphological and interfacial properties of diatom silica microparticles for drug delivery applications. *Advanced Powder Technology*, 24(4):757-763, 2013.

21. Tao, Z., Toms, B., Goodisman, J. and Asefa, T., Mesoporous silica microparticles enhance the cytotoxicity of anticancer platinum drugs. *ACS nano*, 4(2):789-794, 2010.
22. Zhou, W., Gao, P., Shao, L., Caruntu, D., Yu, M., Chen, J. and O'Connor, C.J., Drug-loaded, magnetic, hollow silica nanocomposites for nanomedicine. *Nanomedicine: Nanotechnology, Biology and Medicine*, 1(3):233-237, 2005.
23. Smith, A.M., Duan, H., Mohs, A.M. and Nie, S., Bioconjugated quantum dots for in vivo molecular and cellular imaging. *Advanced drug delivery reviews*, 60(11):1226-1240, 2008.
24. Tallury, P., Payton, K. and Santra, S., Silica-based multimodal/multifunctional nanoparticles for bioimaging and biosensing applications, *Future Medicine*, 3(4):579-592 2008.
25. Lu, F., Wu, S.H., Hung, Y. and Mou, C.Y., Size effect on cell uptake in well-suspended, uniform mesoporous silica nanoparticles. *Small*, 5(12):1408-1413, 2009.
26. Desai, M.P., Labhasetwar, V., Amidon, G.L. and Levy, R.J., Gastrointestinal uptake of biodegradable microparticles: effect of particle size. *Pharmaceutical research*, 13(12):1838-1845, 1996.
27. Yu, Y., Addai-Mensah, J. and Losic, D., Functionalized diatom silica microparticles for removal of mercury ions. *Science and technology of advanced materials*, 13(1):015008, 2012.
28. Yamasaki, T., Sumioka, K. and Tsutsui, T., Organic light-emitting device with an ordered monolayer of silica microspheres as a scattering medium. *Applied Physics Letters*, 76(10):1243-1245, 2000.
29. Ohashi, M., Shiraki, K. and Tajima, K., Optical loss property of silica-based single-mode fibers. *Journal of Lightwave Technology*, 10(5):539-543, 1992.
30. Tong, L., Gattass, R.R., Ashcom, J.B., He, S., Lou, J., Shen, M., Maxwell, I. and Mazur, E., Subwavelength-diameter silica wires for low-loss optical wave guiding. *Nature*, 426(6968):816, 2003.

31. Ikushima, A.J., Fujiwara, T. and Saito, K., Silica glass: A material for photonics. *Journal of Applied Physics*, 88(3):1201-1213, 2000.
32. Berini, P., Long-range surface plasmon-polariton waveguides in silica. *Journal of Applied Physics*, 102(5):053105, 2007.
33. Meng, F., Elsahati, M., Liu, J. and Richards, R.F., Thermal resistance between amorphous silica nanoparticles. *Journal of Applied Physics*, 121(19):194302, 2017.
34. Foster, R.D. and Walker, R.F., Quantitative determination of crystalline silica in respirable-size dust samples by infrared spectrophotometry. *Analyst*, 109(9):1117-1127, 1984.
35. Boruah, M.J., Gogoi, A. and Ahmed, G.A., Laboratory simulation and modeling of size, shape distributed interstellar graphite dust analogues: A comparative study. *Planetary and Space Science*, 125:27-36, 2016.
36. Boruah, M.J., Gogoi, A., Nath, B.C. and Ahmed, G.A., Light scattering studies of randomly oriented polycrystalline fayalite micro particles as interstellar dust analogues. *Journal of Quantitative Spectroscopy and Radiative Transfer*, 196:213-221, 2017.
37. Hodkinson, J.R., Particle sizing by means of the forward scattering lobe. *Applied optics*, 5(5):839-844, 1966.
38. Vilaplana, R., Moreno, F. and Molina, A., Study of the sensitivity of size-averaged scattering matrix elements of nonspherical particles to changes in shape, porosity and refractive index. *Journal of Quantitative Spectroscopy and Radiative Transfer*, 100(1-3):415-428, 2006.
39. Vaz, M.F. and Fortes, M.A., Grain size distribution: The lognormal and the gamma distribution functions. *Scripta metallurgica*, 22(1):35-40, 1988.
40. Winstanley, J.V. and Adams, M.J., Point visibility meter: a forward scatter instrument for the measurement of aerosol extinction coefficient. *Applied optics*, 14(9):2151-2157, 1975.

41. Kitamura, R., Pilon, L. and Jonasz, M., Optical constants of silica glass from extreme ultraviolet to far infrared at near room temperature. *Applied optics*, 46(33):8118-8133, 2007.
42. Malitson, I.H., Interspecimen comparison of the refractive index of fused silica. *Josa*, 55(10):1205-1209, 1965.
43. Boruah, M.J. and Ahmed, G.A., Visible light scattering properties of irregularly shaped silica microparticles using laser based laboratory simulations for remote sensing and medical applications. *Laser Physics*, 28(1):015701, 2017.